Magnetic field strengths of hot Jupiters from signals of star-planet interactions

Authors: P. Wilson Cauley[1⋆], Evgenya L. Shkolnik[2], Joe Llama[3], and Antonino F. Lanza[4]

Affiliations: [1]University of Colorado Boulder, Laboratory of Atmospheric and Space Sciences, Boulder, CO, USA, [2]Arizona State University, School of Earth and Space Exploration, Tempe, AZ, USA, [3]Lowell Observatory, Flagstaff, AZ, USA, [4]INAF-Osservatorio Astrofisico di Catania, Catania, Italy,⋆email: paca7401@lasp.colorado.edu

Evidence of star-planet interactions in the form of planet-modulated chromospheric emission has been noted for a number of hot Jupiters. Magnetic star-planet interactions involve the release of energy stored in the stellar and planetary magnetic fields. These signals thus offer indirect detections of exoplanetary magnetic fields. Here we report the derivation of the magnetic field strengths of four hot Jupiter systems using the power observed in Ca II K emission modulated by magnetic star-planet interactions. By approximating the fractional energy released in the Ca II K line we find that the surface magnetic field values for the hot Jupiters in our sample range from 20 G to 120 G, $\approx 10-100$ times larger than the values predicted by dynamo scaling laws for planets with rotation periods of $\approx 2-4$ days. On the other hand, these value are in agreement with scaling laws relating the magnetic field strength to the internal heat flux in giant planets. Large planetary magnetic field strengths may produce observable electron-cyclotron maser radio emission by preventing the maser from being quenched by the planet's ionosphere. Intensive radio monitoring of hot Jupiter systems will help confirm these field values and inform on the generation mechanism of magnetic fields in this important class of exoplanets.

The close orbits of hot Jupiters ($a \lesssim 10R_*$ where a is the planet's semimajor axis and R_* is the stellar radius) make it possible for these objects to experience strong interactions with their host stars via tides, collisions with stellar wind particles, accretion of evaporating planetary gas onto the stellar surface, and magnetic reconnection between the stellar and planetary magnetic field lines. Star-planet interactions (SPI) can potentially reveal details about stellar wind properties, for which there are very little data[1], and, most intriguingly, planetary magnetic fields[2,3,4,5,6].

Magnetic fields play a critical role in shielding planetary atmospheres from incoming stellar wind particles and limiting mass loss[7,8,9], a key condition for habitability, and provide information about the composition of planetary interiors[10]. Understanding the magnetic fields of hot Jupiters will aid in the future detection and characterization of the magnetic fields of smaller planets closer to the habitable zone[11]. Most critically, measuring exoplanet magnetic field strengths may break the composition degeneracy for planets with known mass and radius, providing information about the structure and dynamics of the convecting and electrically conducting interior[10].

Magnetic SPI signals can manifest as flux changes in the cores of chromospherically active lines that vary on the same timescale as the planet's orbital period, unlike tidal interactions which appear on timescales of half the orbital period[2]. Evidence of such modulations has been observed in a number of hot Jupiter systems in the chromospheric

emission of Ca II. The first such signal was presented for HD 179949[12]. Followup observations demonstrated similar behavior, strengthening the magnetic SPI interpretation[13,14]. Similar signals have been observed in HD 189733, τ Boo, and υ And[15,16]. A flare signature in excess of phased rotational variations has also been noted in HD 73256[13]. SPI-like modulations have also been observed in optical photometric variations[17,18] and in X-rays[19,20,21]. The observed variable nature of some magnetic SPI signatures can be attributed to the planet passing through regions of differing stellar magnetic field strength and topology[22,23,24].

Chromospheric line flux changes due to magnetic SPI may be used to estimate planetary magnetic field strengths. Scaling laws relating the power in magnetic SPI to planetary and stellar properties have been given by various authors[2,5,25,26]. These power estimates are consistent for a variety of different coronal field cases, although the exact constants change depending on the assumptions made. It was demonstrated that, in the case of a dipolar stellar field, the alignment of the stellar and planetary magnetospheres can have a significant impact on the energy dissipated in the magnetic interaction[5]. An additional source of energy in SPI signals may also be provided by particle outflows from the planet onto the stellar surface[27]. It has also been shown that the decrease of the relative helicity of the stellar field, triggered by the close-in planet, allows the evolution of the stellar magnetic field configuration towards a lower energy state thus making dissipation of its magnetic energy by internal reconnection possible on a global scale[25,26]. This process can release a power up to 2-3 orders of magnitude larger than a pure reconnection at the boundary between the stellar and planetary magnetospheres.

With the exception of a power estimate for the HD 179949 SPI signal and the tentative SPI deviations for HD 73256 and κ^1 Cet[13], no other SPI measurements have been flux-calibrated. This is due to the fact that ground-based high-resolution spectra are difficult to flux calibrate accurately and, in general, absolute fluxes are not necessary to confirm a SPI detection. However, in order to constrain specific SPI models or calculate absolute strengths of exoplanetary magnetic fields, measurements of the power emitted in SPI signals are needed[2,28]. Exoplanet magnetic field strengths derived from SPI signals offer an important comparison for future detections, e.g., from radio observations of electron-cyclotron maser emission with the Low-Frequency Array (LOFAR)[29].

In this paper we present magnetic field strengths for a sample of hot Jupiters with published SPI signals (see Table 1). Using a new flux-calibration method for high-resolution spectra, we convert the observed SPI signals into emitted powers and estimate the total power in the SPI mechanism by applying specific models of magnetic SPI. We find that the field strengths are larger than predicted by rotation scaling relations for planets with rotation periods of $\approx 2-4$ days[3,30,31], as is expected for tidally-locked hot Jupiters, and are comparable to the values suggested by internal heat flux scalings relationships which also account for the extra energy deposition in hot Jupiters. Our results suggest that the heat flux description is the most promising of the models considered for predicting the magnetic fields of hot giant planets.

Ionized calcium SPI signals. We used existing data sets for which the changes in the Ca II K (3933.66 Å) cores have been attributed to SPI due to modulation that is phased with the planet's orbital period and exclude those for which the variability is attributable to

stellar rotation[15] (see Methods for details on the observations). Previously published SPI signals are not, in general, flux-calibrated since they are measured with high-resolution ground-based spectrographs. We used corrected PHOENIX model spectra in order to flux-calibrate the Ca II K SPI variations in our sample (see Methods for details). We then converted the Ca II K fluxes to disk-averaged powers by multiplying by πR_*^2.

We show the flux-calibrated Ca II K residual spectra (top row) and summed residual powers (rows 2 - 4) in Figure 1. We generate the residual spectra by subtracting the average spectrum of the epoch from each individual spectrum. The spectra are velocity-corrected to the rest frame of the observed. We then calculate the residual powers by summing the residual spectrum across a 1.0 Å bin centered on the Ca II K rest wavelength. The bottom row in Figure 1 shows the final SPI signals, i.e., residual powers phased to the planetary orbital period. The red lines are the best-fit sinusoid curves to the SPI signal. We use the sinusoids to estimate the peak power in the signal and orbital phase at which the peak power occurs (see Methods for further details). SPI flux, power, and orbital phase offsets from the sub-planetary point, as well as their 68% confidence intervals, are given in Table 2.

Theories of magnetic SPI. Magnetic SPI signals can be used to estimate the strength of planetary magnetic fields by comparing the observed power with predictions from magnetic SPI models. Several analytical predictions for the power released in magnetic SPI have been developed, the first of which estimated the power by assuming that the available energy is generated entirely in reconnection events between the planetary and stellar magnetospheres[2]. It was shown that the power (*P*) at the boundary between the stellar and planetary magnetospheres is

$$P = \gamma \frac{\pi}{\mu} R_{\mathsf{p}}^2 B_*^{4/3} B_{\mathsf{p0}}^{2/3} v_{\mathsf{rel}} \quad (1)$$

where R_{p} is the planetary radius, B_* is the magnitude of the stellar magnetic field at the orbital distance of the planet, B_{p0} is the planetary surface magnetic field at the pole, v_{rel} is the relative velocity between the planet and the stellar magnetic field lines at the planet's orbital distance, μ is the magnetic permeability of free space, and $0 < \gamma < 1$ is an efficiency factor that depends on the relative angle of the stellar and planetary magnetospheres[25,26]. Assuming $\gamma = 0.5$, it was demonstrated[26] that magnetic reconnection alone produces powers $\approx 2-3$ orders of magnitude lower than the $\approx 10^{20}$ W estimate for the SPI signal observed around HD 179949[13]. Even if we assume $\gamma = 1$, $R_{\mathsf{p}} = 1 R_{\mathsf{J}}$, $B_* = 0.005$ G, $B_{\mathsf{p0}} = 100$ G, and $v_{\mathsf{rel}} = 150$ km s^{-1} we find a total power of $\approx 2 \times 10^{18}$ W, two orders of magnitude lower than the observed Ca II K powers. Planetary field strengths of order $\sim 10^4$ G are needed to reach the observed powers. Because of this, we do not further consider the reconnection scenario as a viable model.

Alfvén wing SPI models have also been explored[5,32]. It was found for HD 179949 b that values of the planetary magnetic field strength $\approx 4000\times$ greater than Jupiter's magnetic field strength are needed to reproduce the 10^{20} W estimated for the observed Ca II SPI signal[13]. A variety of Alfvén wing scenarios were investigated for hot massive planets, including the importance of the alignment between stellar and planetary magnetospheres, and scaling laws were generated which estimated the energy available in each case[5]. For

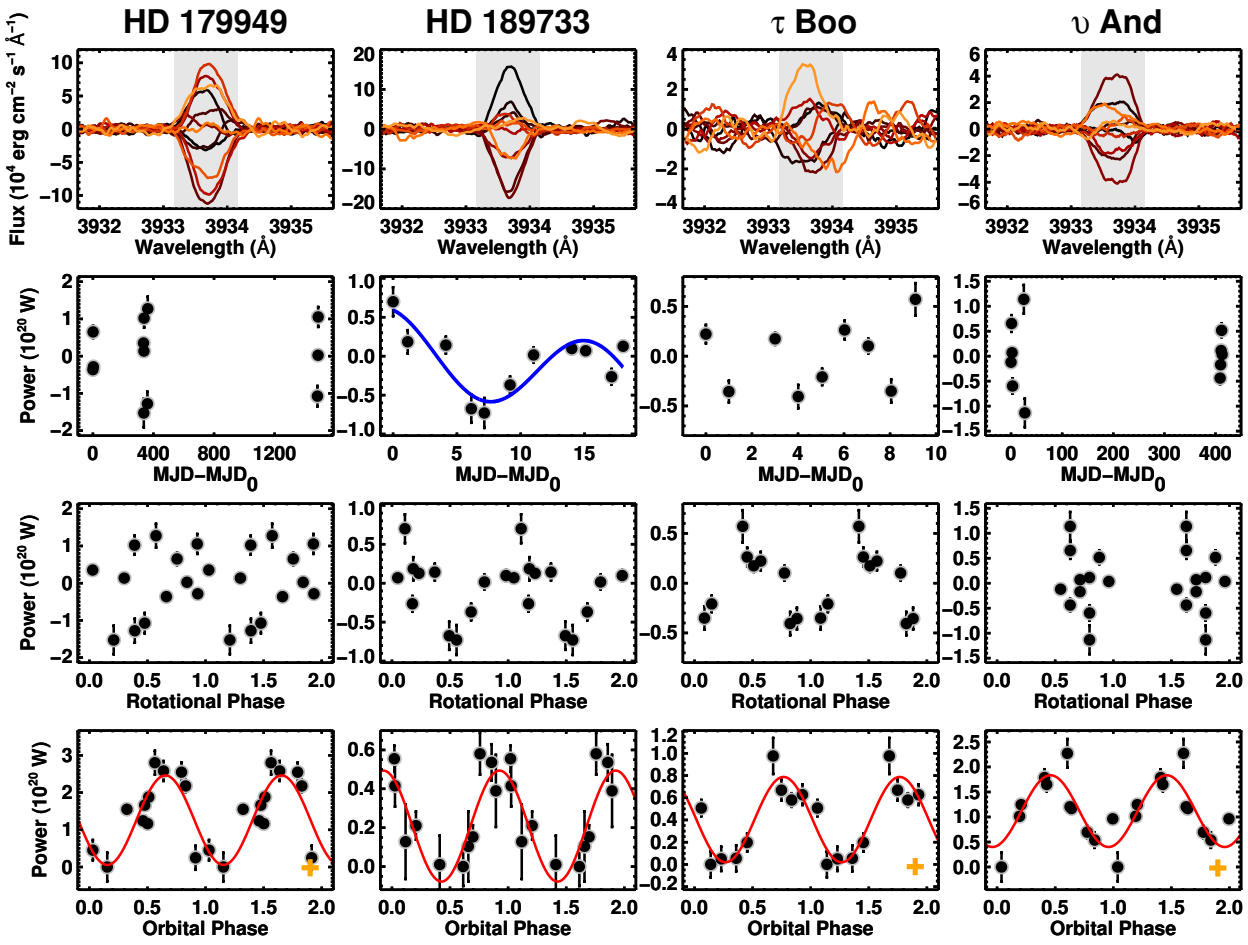

Figure 1: Ca II K residual spectra (top row), summed residual power as a function of time (second row) and stellar rotational phase (third row), and summed residual power as a function of planetary orbital phase (bottom row). The colors in the top row represent different nightly observations: black is earlier in time and red is more recent (see Supplementary Table 1). The residual spectra are smoothed by twenty pixels for clarity and the line core flux integration range is shown in gray. The blue curve in the rotational phase panel for HD 189733 is the best-fit sinusoid to the rotational modulation[16]. Note that τ Boo is synchronously rotating with its planet. The best-fit sinusoids to the orbitally phased data are shown in red. Objects marked with an orange cross do not have their rotational modulation removed. Uncertainties are 1-σ values and are quadrature sums of the residual flux uncertainties. The power uncertainties include the uncertainty of the stellar radius.

most cases, it was found that the available power is $\approx 10^{19}$ W, slightly lower than needed to explain the powers derived here, especially given the fact that the measured powers include only that emitted by the Ca II K line which is a fraction of the total emitted power.

In another possible scenario, planets may increase the star's magnetic helicity, which is a measure of the twisting of coronal field lines and is generally conserved during the coronal field evolution putting a constraint on the possible energy release process. Power estimates have been computed for variations in coronal magnetic field helicity as induced by the passage of the massive planet through the stellar magnetosphere[26]. It was found that both linear and non-linear force-free fields provide a similar amount of power compared with the case of pure reconnection and thus are also inadequate to explain the observations.

The most promising scenario for producing the necessary power, which was explored analytically with the goal of estimating how energy generated in magnetic SPI can cause evaporation of planetary material, is the Poynting flux across the base of a magnetic flux tube connecting the planetary surface to the stellar surface[33]. The power is generated by continuous stretching of the magnetic footprint on the stellar surface due to the relative motion between the planet and stellar magnetosphere. It was shown that in this case the available power is approximately

$$P \approx \frac{2\pi}{\mu} f_{AP} R_{\rm p}^2 B_{\rm p0}^2 v_{\rm rel} \qquad (2)$$

where R_p, $B_{\rm p0}$, μ, and $v_{\rm rel}$ have the same meanings as in equation (1) and f_{AP} is the fraction of the planetary hemisphere covered by flux tubes[33]. In this case, the total available power is $\approx 10^{20} - 10^{21}$ W, sufficient to explain the powers measured here. We consider this the most likely description of magnetic SPI for hot giant planets as it is the only one that predicts the observed emitted powers. We note that similar powers are obtained in numerical simulations of hot giant planets involving similar magnetic interactions with their host stars[28].

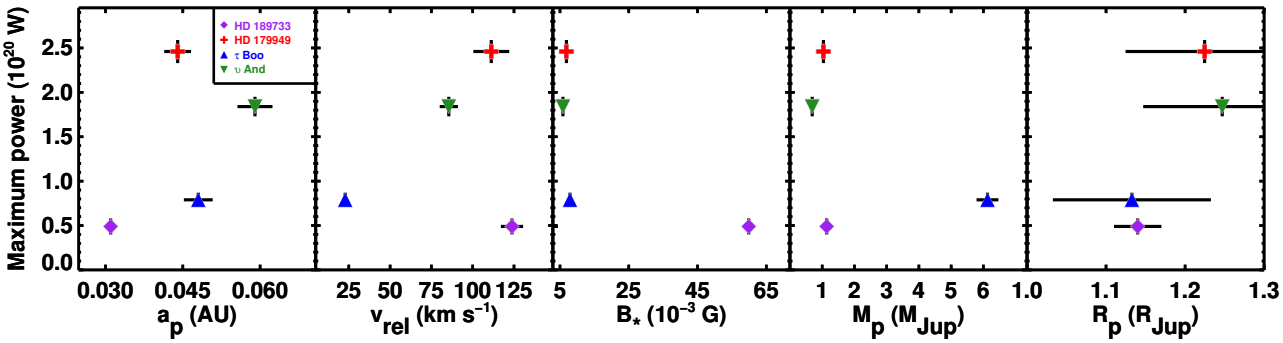

Figure 2: Observed powers in the Ca II K line residuals as a function of relevant magnetic SPI parameters. The powers range from ≈ 0.5 to 2.2 10^{20} W. Note that B_* is the stellar magnetic field strength at the orbital distance of the planet. Uncertainties for the system parameters are 1-σ literature values. There are no obvious correlations between any of the individual parameters and the measured powers.

Figure 2 shows the maximum Ca II K power as a function of relevant SPI parameters from equation (2). There is no clear trend with any single system parameter, although the two planets with the largest radii have the highest powers. The range of observed powers only varies by a factor of ≈ 5, suggesting that the physical mechanism responsible for producing the Ca II K variations is roughly the same in all systems. If, for example, the reconnection scenario given by equation (1) was producing the SPI signal in one system and the flux tube scenario from equation (2) was active in another, we might expect to see powers that differ by a factor of $\approx 100 - 1000$.

Another indicative feature of the observed magnetic SPI signals is the phase at which the power is greatest: for all objects the peak power is reached between $\phi_{\mathsf{max}} \approx 0.5 - 0.9$, which corresponds to a phase lag between the planet and the induced hot spot on the star of $\Delta\phi \approx 180^\circ$ and 30°. These values are consistent with certain cases of the linear and non-linear force-free flux tube models[26], although the large phase lag observed for υ And is difficult to reproduce with either model. Regardless of the specific model interpretation, it is notable that three of the four objects have phase lags within a fairly narrow range.

Planetary magnetic field strengths. With the Ca II K powers, we can calculate absolute field strengths for the planets using the favored flux tube SPI model. All of the quantities in equation (2) are known or can be well estimated and thus we can solve for B_{p0} for each planet. In equation (2), f_{AP} depends on the ratio B_*/B_{p0} and so equation (2) must be solved numerically. For the field strengths we derive here, $f_{\mathsf{AP}} = 0.02 - 0.20$.

Since the observed Ca II K power is a lower limit to the total power produced by the SPI mechanism we need to estimate the fraction of the total SPI energy radiated away in Ca II K. We accomplish this by comparing the SPI emission to moderate solar flares, which are also powered by the release of magnetic energy. Using the modeled dissipated energies for M-class solar flares[34], which comprise $\approx 10\%$ of measured X-ray flares[35], and the energy radiated in Ca II K for an M-class flare ($\approx 2.5 \times 10^{29}$ ergs[36]), we estimate that Ca II K emits energy equal to $0.21\% \pm 0.08\%$ of the total energy dissipated in the flare, where the uncertainty is the standard deviation of the M-class flare dissipated energies (assuming a constant value for the emitted Ca II K energy). We calculate the planetary field strengths within the $\pm 1\sigma$ boundaries for the Ca II K conversion fraction. We note that the fraction of optical emission line energy radiated in Ca II K was found to be $\approx 14\%$ of the total energy observed during a flare on HD 189733, which emitted a total of $> 9 \times 10^{31}$ ergs[37]. The same measurement of Ca II K energy in the aforementioned M-class solar flare, which emitted $\approx 2 \times 10^{30}$ ergs, is 13%[36], suggesting that the fraction of energy emitted by Ca II K is consistent across this range of flare energies.

In Table 3 we report magnetic field strengths of the sample for different values of ϵ, the fraction of the total dissipated energy radiated away in Ca II K. We give the $\epsilon = 100\%$ values as a lower-limit reference. We derive the 1σ uncertainties by propagating the parameter errors from Table 1 in quadrature. Note that, with the exception of υ And b, the uncertainties on individual values of B_{p0} are similar to the spread in B_{p0} for different values of ϵ. The measurement uncertainty for υ And b is $\approx 90\%$ of the planetary field strength value due to the large uncertainty in the stellar magnetic field.

We also include in Table 3 (last row) the surface polar planetary field strengths calculated using the recent scaling relation for hot planets which includes the extra heat from

the central star[38]. Building on previous work which showed that the magnetic field strength of giant planets depends on their internal heat flux[39,40], magnetic field strengths were estimated for hot Jupiters which receive an incident flux $\geq 2 \times 10^8$ erg s^{-1} cm^{-2} and have $R_\mathsf{p} \geq R_\mathsf{J}$[38]. This model included the excess luminosity that results from heating by the central star[41]. Since the magnetic field scaling law relies on the internal heat flux of the planet[39], the field strengths including heating from the central star are $\approx 4-5\times$ larger than the nominal values which only consider the cooling of the planet over time[40]. The models which include the extra heating assume for simplicity that the heat is deposited at the center of the planet. Off-center heat deposition may disrupt convective flows in the planet interior or reduce the efficiency of conversion to magnetic energy, reducing the magnetic field strength. Thus the extra heat values are likely upper limits. On the other hand, it has been noted that the dynamo generation region in giant planets may be close to the surface[30], which would allow more of the deposited heat to contribute to the generation of a magnetic field.

We plot the planetary field strengths from equation (2) against the planetary field strengths calculated with the extra stellar heating models[38] in Figure 3. There is some agreement between the SPI-derived fields and those from the scaling relations which include the additional heat flux from the star. More important is the fact that the values of B_{p0} we derive here are $\approx 2-8\times$ larger than predicted by rotation scaling and internal heat flux evolution without considering the extra energy deposited into hot planet interiors by their host stars[40]. We suggest that the correspondence shown here between the field strengths derived from the flux tube SPI scenario and the extra heat deposition model supports the idea of hot massive planets hosting much stronger magnetic fields than would be expected from only considering the thermal evolution of the planet and their slow rotation[30,31]. More flux-calibrated SPI detections are needed for planets with known radii (i.e., transiting planets) in order to enlarge the comparison sample.

Our results are in contrast with the small magnetic moments derived for hot planets using models of exospheric Lyman-α absorption. A magnetic moment of $\approx 0.1\mu_{\mathsf{Jup}}$, where μ_{Jup} is the magnetic moment of Jupiter, was found for HD 209458 b[42]. The extra heat deposition models estimate a polar surface magnetic field strength for HD 209458 b of ≈ 49 G[38], approximately three times stronger than Jupiter's surface field. Similarly, the magnetic moment for the hot Neptune GJ 436 b was estimated to be $\approx 0.16\mu_{\mathsf{Jup}}$[43]. These models, however, rely on a number of highly uncertain parameters (e.g., planetary mass loss rate and stellar wind density) and, in the case of HD 209458 b, a low-signal-to-noise Lyman-α transmission spectrum.

The large planetary field strengths we find for our sample have important consequences for the detection of radio emission from the planets' magnetospheres. It has been suggested that the dense ionospheres of some hot Jupiters may quench any radio waves generated by the electron-cyclotron maser instability (ECMI) since the plasma frequency will be greater than that of the radio emission[44,45]. However, this is generally only the case for weak planetary field strengths of the order $\approx 1-10$ G and planets with extended ionospheres[46]. For the planetary field strengths we find here, conditions are more favorable for the generation and escape of radio waves produced by the ECMI. The peak radio frequencies emitted by the ECMI for our sample, which is $\nu_{\mathsf{peak}} \approx 2.8 B_{\mathsf{p0}}$ MHz[3], are 56, 240, 327, and 232 MHz for HD 189733 b, HD 179949 b, τ Boo b, and υ And

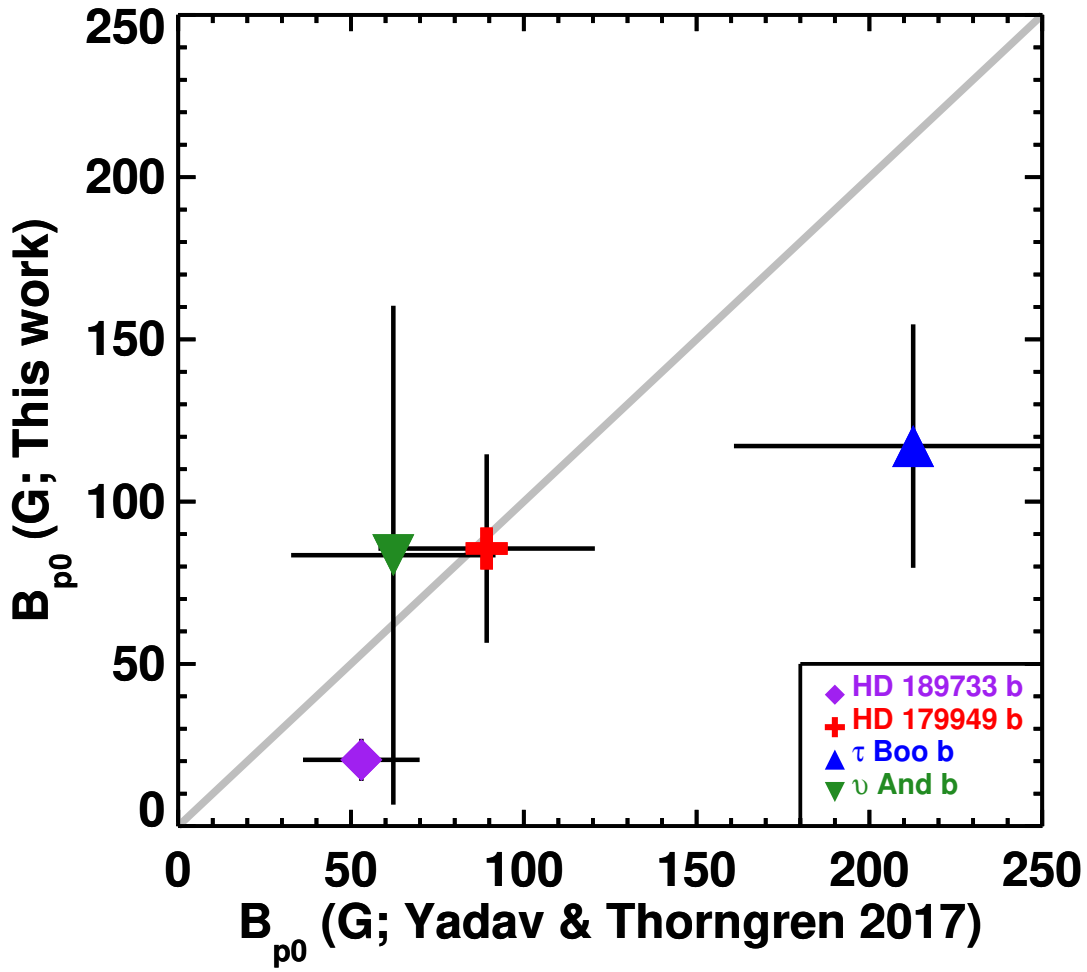

Figure 3: Magnetic field strengths from equation (2) and those calculated using the extra heat deposition models[38] for the case of $\epsilon = 0.2\%$ from Table 3. The gray line is the line of equal values. Uncertainties are 1-σ values and are derived by propagating the parameter and power errors in quadrature. There is some correspondence between the SPI field strengths and those from the extra heat deposition models, supporting internal heat flux descriptions of magnetic field generation in hot planets.

b, respectively. Radio observations of our sample near these frequencies will be useful in confirming our derived field strengths which will aid in illuminating the most dominant physical parameters for predicting giant planet magnetic fields.

Methods

Observations and data reduction. High-resolution spectra ($R \approx 65,000-110,000$) of our targets (Supplementary Table 1) were obtained with NARVAL on the 2-meter Télescope Bernard Lyot (TBL) or Gecko or ESPaDOnS on the 3.6-meter Canada France Hawaii Telescope (CFHT). We give the references for the original publications in Supplementary Table 1. Data reduction details can be found in these references but a brief summary is given here. Standard reduction steps were performed for all exposures, including bias subtraction, or dark subtraction in the case of the Gecko data, flat fielding, and wavelength calibration using a reference lamp exposure. All data from ESPaDOnS and NARVAL were reduced using the automated pipeline `LIBRE-ESPRIT`. The typical signal-to-noise per pixel in the continuum near Ca II K for an average nightly spectrum ranges from ≈ 300 up to ≈ 3000. All spectra are corrected for the Earth's heliocentric motion, the system's radial velocity, and the radial velocity induced by the planet on the star.

All of the stellar and planetary parameters and their uncertainties are given in Table 1. Uncertainties for the orbital periods and semi-major axes are negligible and are omitted from the analysis. We estimate the radii of the non-transiting planets using a probabilistic mass-radius relationship[56]. For hot Jupiters, the radius is also a function of incident stellar flux, with more highly irradiated planets having larger radii for a given mass[41]. This results in a large radius spread of $\approx 15\%$ at a particular mass[56] since most of the Jupiter-mass planets with known radii are hot Jupiters. We thus consider the planetary radii to be uncertain at the level of 15%.

Calculating the Ca II K fluxes. High-resolution spectra are not, in general, flux calibrated, which makes it impossible to use the SPI signals to derive planetary magnetic field strengths. Estimates of the surface flux can be obtained by using the absolute fluxes from PHOENIX model spectra of the same $T_{\rm eff}$. These PHOENIX models have been used in a number of previous studies for a similar purpose[57,58] and are currently the gold-standard in stellar photosphere models for FGKM main-sequence stars.

In order to estimate the Ca II K surface fluxes of our objects, we used a grid of PHOENIX model spectra[59] with $\log g = 4.5$ and [Fe/H] $= 0.0$. Before applying the PHOENIX spectra to the data, it is important to understand how well the model surface fluxes predict measured flux values.

To accomplish this we retrieved the latest version of the Next Generation Spectral Library (NGSL) from the MAST database[1]. The NGSL contains 374 stars with spectra covering $\lambda = 2000 - 10000$ Å at $R \approx 1000$, observed using the Space Telescope Imaging Spectrograph onboard the *Hubble Space Telescope*. To ensure that we only used NGSL stars with well-determined parameters, we cross-referenced the NGSL objects with those from the PASTEL catalog[60], resulting in 295 matches. Since our targets are comprised of main sequence FGK stars, we only selected objects from the remaining sample with

[1] https://archive.stsci.edu/prepds/stisngsl/

4500 K $< T_{\rm eff} <$ 7000 K, $4.1 <$ log$g < 4.7$, and $-1.0 <$ [Fe/H] < 1.0. These cuts resulted in 38 final objects.

Converting observed fluxes to surface fluxes requires knowledge of the object's distance and radius. All of the final 38 objects have well known distances, as they all reside $d_* < 100$ pc from the sun. In order to derive radii for the sample, we used the $T_{\rm eff}$ and log$g$ values from the PASTEL catalog and a recent $T_{\rm eff} - M_*$ relationship[61]. We then solved for R_* using the measured log$g$ values and the interpolated M_* values.

Once the NGSL spectra were converted into surface flux, we took the mean flux value in two continuum bands between 3885-3915 and 3980-4010 Å. We performed the same steps to the PHOENIX model spectra, which we convolved down to the spectral resolution of the NGSL spectra. An example of a comparison between the NGSL star HD 21742 with $T_{\rm eff} = 5160$ K and the corresponding PHOENIX model of the same $T_{\rm eff}$ is shown in Supplementary Figure 1. The resulting mean NGSL and PHOENIX model fluxes are shown in the top panel of Supplementary Figure 2; the bottom panel shows the ratio of the model fluxes to the NGSL fluxes.

Overall, the measured fluxes are well approximated by the PHOENIX models. However, there is a trend in the flux ratio: the models tend to over-predict the measured values for $T_{\rm eff} \lesssim 5500$ K by $\approx 10 - 30\%$ and only slightly over-predict them for larger $T_{\rm eff}$. A typical example of the over-predicted flux is shown in Supplementary Figure 1. To account for this trend in $T_{\rm eff}$ we fit a power law to the $F_{\rm mod}/F_{\rm CaII}$ values in the lower panel. The fit is performed using an MCMC procedure based on affine-invariant sampling[62,63]. The best-fit result and 68% confidence intervals are shown with the solid orange line and gray band, respectively. This fit is applied to all of the Ca II flux derivations for our SPI sample. We note that for most objects the correction is $< 15\%$.

The exact cause of the larger model discrepancies at lower $T_{\rm eff}$ is unknown. The NGSL spectra were observed with the $52'' \times 0.2''$ slit and there is no evidence of a systematic error in the flux calibration as a function of stellar color. PHOENIX model surface fluxes between 3900 Å and 4000 Å for log$g = 4.0 - 5.0$ only differ by at most 15%, ruling out the constant log$g$ of the models as the cause. The difference is likely due to the LTE treatment of most atomic species in the models, which can significantly change the flux in the wings of strong lines, such as Ca II K.

Emitted power estimates. All of the published spectra we use were continuum normalized. In order to flux-calibrate a spectrum, a flux correction factor is needed that is a function of wavelength across the desired range. Our approach was as follows:

1. Interpolate between PHOENIX spectra to produce a model spectrum with approximately the same $T_{\rm eff}$ as the object.

2. Perform a linear fit to the continuum surrounding the Ca II H and K lines of the model spectrum.

3. Multiply the normalized object spectrum by the linear flux correction factor.

4. Multiply the flux-calibrated object spectrum by the power law adjustment factor.

5. Subtract the mean flux-calibrated spectrum of the epoch from all individual spectra from the same epoch.

6. Sum the residual core flux across a 1 Å band centered on the rest wavelength of the line.

7. Multiply the core flux by πR_*^2 to find the power averaged over the observable stellar disk.

We show an example of steps 1-3 in the flux calibration process in Supplementary Figure 3. The Gecko spectra for HD 179949 and υ And cover a subset of the Ca II H and K order of ESPaDOnS and NARVAL spectra and cannot be normalized in the same way using step 2. We made minor continuum corrections to the Gecko orders by multiplying the continuum by the ratio between the Gecko spectrum and an average spectrum of the same object taken with ESPaDOnS from a separate epoch. We then applied the flux calibration vector from the ESPaDOnS epochs to the Gecko spectra, which then have the same stellar continuum shape as the ESPaDOnS spectra.

We note that the scatter of the observed fluxes compared with the power law fit in Supplementary Figure 2 is larger ($\approx 15\%$) than the spread in surface flux of models within the $T_{\rm eff}$ uncertainty range ($\approx \pm 50$ K). Thus we do not consider the linear continuum fit or $T_{\rm eff}$ as sources of uncertainty in the surface fluxes.

We generated the residual spectra by subtracting the flux-calibrated average spectrum for the epoch from each individual spectrum from the same epoch. For example, there are three separate observing epochs for HD 179979. Any small offsets from zero, which are typically $5 - 10\%$ of the residual flux level, in the continuum are then removed with a low order polynomial. Note that we only calculated residual fluxes for the Ca II K line due to the higher signal-to-noise for some objects and the strong correlation between Ca II H and K residual measurements[12]. Once the spectra are corrected, the residual Ca II K fluxes are summed across a 1.0 Å wide band centered on 3933.66 Å. We then converted the fluxes to powers by multiplying by πR_*^2.

We calculated the uncertainties on the power estimates by combining in quadrature the 1σ flux error from the residual spectra as measured outside of the line core with the uncertainty in the stellar radius and a 15% uncertainty in the model flux correction factor. The correction factor uncertainty is the standard deviation of the residuals to the power law fit in Supplementary Figure 2.

We subtracted rotational modulation attributed to the star from the residuals for HD 189733[16]. HD 179949 and υ And do not show evidence of rotational modulation in the epochs chosen for this analysis. τ Boo b has an orbital period similar to its star's rotational period. However, photometric variations observed for τ Boo can more plausibly be attributed to the planet rather than stellar rotation due to their persistence across multiple years and consistency with the planetary orbital period and phase[17]. Based on this evidence it is most likely that the Ca II K variations are due to the planet.

We fit a sinusoid to the orbitally phased signals in order to derive estimates of the maximum power and phase offset. Although SPI variations may not be fully described by a simple sinusoid, we chose this functional form to avoid over-fitting the small number of data points. The period was fixed to the planet's orbital period, leaving the phase offset

and amplitude as the free parameters. The fits were performed with the same MCMC procedure used to derive the flux correction factor. We chose the peak in the model sine curve and its phase offset, along with each parameter's 68% confidence intervals, as the maximum power and phase offset for the observed SPI signals. The mean power was taken directly from the data where the uncertainty is simply the standard deviation of the mean.

Data Availability. The data that support the plots within this paper and other findings of this study are available from the corresponding author upon reasonable request. The reduced spectra used here are also publicly available via the PolarBase archive and the CFHT data archive.

References

1. Wood, B. E., Müller, H R, Zank, G. P, Linsky, J. L, Redfield, S. New Mass-Loss Measurements from Astrospheric Lyα Absorption. *Astrophys. J.* **628,** L143-L146 (2005)

2. Cuntz, M., Saar, S., & Zdzislaw, E. On Stellar Activity Enhancement Due to Interactions with Extrasolar Giant Planets. *Astrophys. J.* **533,** L151-L154 (2000)

3. Stevens, I. R. Magnetospheric radio emission from extrasolar giant planets: the role of the host stars. *Mon. Not. R. Astron. Soc.* **356,** 1053-1063 (2005)

4. Vidotto, A. A., Jardine, M., & Helling Ch. Transit variability in bow shock-hosting planets. *Mon. Not. R. Astron. Soc.* **414,** 1573-1582 (2011)

5. Strugarek, A. Assessing Magnetic Torgues and Energy Fluxes in Close-in Star-Planet systems. *Astrophys. J.* **833,** 140-152 (2016)

6. Rogers, T. M., & McElwaine, J. N. The Hottest Hot Jupiters May Host Atmospheric Dynamos. *Astrophys. J. Lett.* **841,** L26-L32 (2017)

7. Cohen, O., et al. The Interaction of Venus-like, M-dwarf Planets with the Stellar Wind of Their Host Star. *Astrophys. J.* **806,** 41-51 (2015)

8. Jakosky, B. M., et al. Mars' atmospheric history derived from upper-atmosphere measurements of ^{38}Ar/^{36}Ar. *Science* **355,** 1408-1410 (2017)

9. Blackman, E. G., & Tarduno, J. A. Mass, energy, and momentum capture from stellar winds by magnetized and unmagnetized planets: implications for atmospheric erosion and habitability. *Mon. Not. R. Astron. Soc.* **481,** 5146-5155 (2018)

10. Lazio, T. J. W., et al. 2016, Planetary Magnetic Fields: Planetary interiors and habitability, final report prepared by the Keck Institute of Space Studies

11. Shkolnik, E. L., & Llama, J. *Handbook of Exoplanets* Signatures of Star-Planet Interactions (Springer, 2017)

12. Shkolnik, E., Walker, G. A. H., & Bohlender, D. A. Evidence for Planet-induced Chromospheric Activity on HD 179949. *Astrophys. J.* **597,** 1092-1096 (2003)

13. Shkolnik, E., Walker, G. A. H., Bohlender, D. A., Gu, P.-G., & Kürster, M. Hot Jupiters and Hot Spots: The Short- and Long-Term Chromospheric Activity on Stars with Giant Planets. *Astrophys. J.* **622,** 1075-1090 (2005)

14. Gurdemir, L., Redfield, S., & Cuntz, M. Planet-Induced Emission Enhancements in HD 179949: Results from McDonald Observations. *Publ. Astron. Soc. Pac.* **29,** 141-149 (2012)

15. Shkolnik, E., Bohlender, D. A., Walker, G. A. H., & Collier Cameron, A. The On/Off Nature of Star-Planet Interactions. *Astrophys. J.* **676,** 628-638 (2008)

16. Cauley, P. W., Shkolnik, E. S., Llama, J., Bourrier, V., & Moutou, C. Evidence of Magnetic Star-Planet Interactions in the HD 189733 System from Orbitally Phased Ca II K Variations. *Astron. J.* **156,** 262-273 (2018)

17. Walker, G. A. H., et al. MOST Detects Variability on τ Bootis A Possibly Induced by its Planetary Companion. *Astron. Astrophys.* **482,** 691-697 (2008)

18. Pagano, I., et al. CoRoT-2a Magnetic Activity: Hints for Possible Star-Planet Interaction. *Earth Moon and Planets* **105,** 373-378 (2009)

19. Scandariato, G., et al. A Coordinated Optical and X-ray Spectroscopic Campaign on HD 179949: Searching for Planet-Induced Chromospheric and Coronal Activity. *Astron. Astrophys.* **552,** 7-20 (2013)

20. Maggio, A., et al. Coordinated X-Ray and Optical Observations of Star-Planet Interaction in HD 17156. *Astrophy. J.* **811,** L2-L7 (2015)

21. Pillitteri, I., et al. FUV Variability of HD 189733. Is the Star Accreting Material from its Hot Jupiter? *Astrophys. J.* **805,** 52-70 (2015)

22. Cranmer, S. R., & Saar, S. H. Exoplanet-Induced Chromospheric Activity: Realistic Light Curves from Solar-type Magnetic Fields. Preprint at https://arxiv.org/pdf/astro-ph/0702530.pdf (2007)

23. Llama, J., et al. Exoplanet Transit Variability: Bow Shocks and Winds Around HD 189733 b. *Mon. Not. R. Astron. Soc.* **436,** 2179-2187 (2013)

24. Fares, R., et al. A Small Survey of the Magnetic Fields of Planet-Host Stars. *Mon. Not. R. Astron. Soc.* **435,** 1451-1462 (2013)

25. Lanza, A. F. Stellar Coronal Magnetic Fields and Star-Planet Interaction. *Astron. Astrophys.* **505,** 339-350 (2009)

26. Lanza, A. F. Star-Planet Magnetic Interaction and Activity in Late-Type Stars with Close-In Planets. *Astron. Astrophys.* **544,** 23-39 (2012)

27. Cohen, O., et al. The Dynamics of Stellar Coronae Harboring Hot Jupiters. I. A Time-Dependent Magnetohydrodynamic Simulations of the Interplanetary Environment in the HD 189733 Planetary System. *Astrophys. J.* **733,** 67-79 (2011)

28. Scharf, C. A. Possible Constraints on Exoplanet Magnetic Field Strengths from Planet-Star Interaction. *Astrophys. J.* **722,** 1547-1555 (2010)

29. van Haarlem, M. P., et al. LOFAR: The LOw-Frequency ARray. *Astron. Astrophys.* **556,** 2-55 (2013)

30. Zaghoo, M., & Collins, G. W. Size and Strength of Self-Excited Dynamos in Jupiter-like Extrasolar Planets. *Astrophys. J.* **862,** 19-29 (2018)

31. Sánchez-Lavega, A. The MAgnetic Field in Giant Extrasolar Planets. *Astrophys. J.* **609,** L87-L90 (2004)

32. Saur, J., Grambusch, T., Duling, S., Neubauer, F. M., & Simon, S. Magnetic Energy Fluxes in Sub-Alfvénic Planet-Star and Moon-Planet Interactions. *Astron. Astrophys.* **552,** 119-139 (2013)

33. Lanza, A. F. Star-Planet Magnetic Interactions and Evaporation of Planetary Atmospheres. *Astron. Astrophys.* **557,** 31-44 (2013)

34. Aschwanden, M. J., Xu, Y., & Jing, J. Global Energetics of Solar Flares. I. Magnetic Energies. *Astrophys. J.* **797,** 50-85 (2014)

35. Veronig, A., Temmer, M., Hanslmeier, A., Otruba, W., & Messerotti, M. Temporal Aspects and Frequency Distributions of Solar Soft X-ray Flares. *Astron. Astrophys.* **382,** 1070-1080 (2002)

36. Johns-Krull, C. M., Hawley, S. L., Basri, G., & Valenti, J. A. Hamilton Echelle Spectroscopy of the 1993 March 6 Solar Flare. *Astrophys. J. Supp.* **112,** 221-243 (1997)

37. Klocová, T., Czesla, S., Khalafinejad, S., Wolter, U., & Schmitt, J. H. M. M. Time-Resolved UVES Observations of a Stellar Flare on the Planet Host HD 189733 During Primary Transit. *Astron. Astrophys.* **607,** 66-78 (2017)

38. Yadav, R. K., & Thorngren, D. P. Estimating the Magnetic Field Strengths in Hot Jupiters. *Astrophys. J. Lett.* **849,** L12-L16 (2017)

39. Christensen, U. R., Holzwarth, V., & Reiners, A. Energy Flux Determines Magnetic Field Strength of Planets and Stars. *Nature* **457,** 167-169 (2009)

40. Reiners, A., & Christensen, U. R. A Magnetic Field Evolution Scenario for Brown Dwarfs and Giant Planets. *Astron. Astrophys.* **522,** 13-20 (2010)

41. Thorngren, D. P., & Fortney, J. J. Bayesian Analysis of Hot-Jupiter Radius Anomalies: Evidence for Ohmic Dissipation? *Astron. J.* **155,** 214-224 (2018)

42. Kislyakova, K. G., Holmström, M., Lammer, H., Odert, P., & Khodachenko, M. L. Magnetic Moment and Plasma Environment of HD 209458b as Determined from Lyα Observations. *Science* **346,** 981-984 (2014)

43. Bourrier, V., Lecavelier des Etangs, A., Ehrenreich, D., Tanaka, Y. A., & Vidotto, A. A. An Evaporating Planet in the Wind: Stellar Wind Interactions with the Radiatively Braked Exosphere of GJ 436 b. *Astron. Astrophys.* **591,** 121-135 (2016)

44. Weber, C., et al. How Expanded Ionospheres of Hot Jupiters Can Prevent Escape of Radio Emission Generated by the Cyclotron Maser Instability. *Mon. Not. R. Astron. Soc.* **469,** 3505-3517 (2017)

45. Daley-Yates, S., & Stevens, I. R. Inhibition of the Electron Cyclotron Maser Instability in the Dense Magnetosphere of a Hot Jupiter. *Mon. Not. R. Astron. Soc.* **479,** 1194-1209 (2018)

46. Weber, C., et al. Supermassive Hot Jupiters Provide More Favourable Conditions for the Generation of Radio Emission via the Cyclotron Maser Instability - A Case Study Based on Tau Bootis b. *Mon. Not. R. Astron. Soc.* **480,** 3680-3688 (2018)

47. Butler, R. P., et al. Catalog of Nearby Exoplanets. *Astrophys. J.* **646,** 505-522 (2006)

48. Fares, R., et al. Magnetic Field, Differential Rotation and Activity of the Hot-Jupiter-Hosting Star HD 179949. *Mon. Not. R. Astron. Soc.* **423,** 1006-1017 (2012)

49. Fares, R., et al. MOVES - I. The Evolving Magnetic Field of the Planet-Hosting Star HD 189733. *Mon. Not. R. Astron. Soc.* **471,** 1246-1257 (2017)

50. Bouchy, F., et al. ELODIE Metallicity-Biased Search for Transiting Hot Jupiters. II. A Very Hot Jupiter Transiting the Bright K Star HD 189733. *Astron. Astrophys.* **444,** L15-L19 (2005)

51. Winn, J., et al. The Transit Light Curve Project. V. System Parameters and Stellar Rotation Period of HD 189733. *Astron. J.* **133,** 1828-1835 (2007)

52. Boisse, I., et al. Stellar Activity of Planetary Host Star HD 189733. *Astron. Astrophys.* **495,** 959-966 (2009)

53. Catala, C., Donati, J.-F., Shkolnik, E. S., Bohlender, D., & Alecian, E. The Magnetic Field of the Planet-Hosting Star τ Bootis. *Mon. Not. R. Astron. Soc.* **374,** L42-L46 (2007)

54. Jeffers, S. V., et al. The Relation Between Stellar Magnetic Field Geometry and Chromospheric Activity Cycles - II. The Rapid 120-Day Magnetic Cycle of τ Bootis. *Mon. Not. R. Astron. Soc.* **479,** 5266-5271 (2018)

55. Marsden, S. C., et al. A BCool Magnetic Snapshot Survey of Solar-Type Stars. *Mon. Not. R. Astron. Soc.* **444,** 3517-3536 (2014)

56. Chen, J., & Kipping, D. Probabilistic Forecasting of the Masses and Radii of Other Worlds. *Astrophys. J.* **834,** 17-30 (2017)

57. Mittag, M., Schmitt, J. H. M. M., & Schröder, K.-P. Ca II H+K Fluxes from S-Indices of Large Samples: A Reliable and Consistent Conversion Based on PHOENIX Model Atmospheres. *Astron. Astrophys.* **549,** 117-129 (2013)

58. Scandariato, G., et al. HADES RV Programme with HARPS-N at TNG. IV. Time Resolved Analysis of the Ca II H&K and Hα Chromospheric Emission of Low-Activity Early-Type M Dwarfs. *Astron. Astrophys.* **598,** 28-42 (2017)

59. Husser, T.-O., et al. A New Extensive Library of PHOENIX Stellar Atmospheres and Synthetic Spectra. *Astron. Astrophys.* **553,** 6-15 (2013)

60. Soubiran, C., Le Campion, J.-F., Brouillet, N., & Chemin, L. The PASTEL Catalogue: 2016 Version. *Astron. Astrophys.* **591,** 118-125 (2016)

61. Eker, Z., et al. Main-Sequence Effective Temperatures from a Revised Mass-Luminosity Relation Based on Accurate Properties. *Astron. J.* **149,** 131-147 (2015)

62. Goodman, J., & Weare, J. Ensemple Samplers with Affine Invariance. *Comm. App. Math. Comp.* **5,** 65-80 (2010)

63. Foreman-Mackey, D., Hogg, D. W., Lang, D., & Goodman, J. emcee: The MCMC Hammer. Preprint at https://arxiv.org/abs/1202.3665 (2012)

Acknowledgments. We thank Travis Barman for insightful discussions concerning details of the PHOENIX models. P.W.C. and E.L.S. acknowledge support from NASA Origins of the Solar System grant No. NNX13AH79G (P. I. Shkolnik). This work has made use of NASA's Astrophysics Data System and used the facilities of the Canadian Astronomy Data Centre operated by the National Research Council of Canada with the support of the Canadian Space Agency.

Author Contributions. This work made use of archived data. E. L. S. was responsible for most of the original observing proposals and data collection. P. W. C. was responsible for the flux calibration and SPI signal analysis, as well as the manuscript preparation. J. L. was responsible for some original SPI signal analysis and also contributed to the manuscript. A. F. L. provided interpretation of the SPI theories and oversight of the theory application. All authors contributed material to the manuscript.

Competing interests. The authors declare no competing interests.

Object	$T_{\rm eff}$ (K)	R_* ($R_\odot$)	$P_{\rm rot}$ (days)	$B_*(r=R_*)$ (G)	$M_{\rm pl}$ ($M_{\rm Jup}$)	$R_{\rm p}$ ($R_{\rm Jup}$)	$P_{\rm orb}$ (days)	$a_{\rm p}$ (AU)	References
HD 179949	6170 ± 50	1.23 ± 0.03	11.0 ± 0.8	3.2 ± 0.3	1.04 ± 0.08	1.22 ± 0.18	3.0925	0.044	47,48
HD 189733	5040 ± 50	0.76 ± 0.01	11.9 ± 0.16	27.0 ± 3.0	1.14 ± 0.03	1.14 ± 0.03	2.2186	0.031	49,50,51,52
τ Boo	6387 ± 50	1.48 ± 0.08	3.7 ± 0.1	2.6 ± 0.2	6.13 ± 0.34	1.13 ± 0.17	3.3124	0.048	47,53,54
υ And	6213 ± 50	1.64 ± 0.04	12.0 ± 0.1	2.5 ± 1.1	0.69 ± 0.06	1.25 ± 0.19	4.6170	0.059	47,55

Table 1: **SPI system parameters.** All uncertainties are 1-σ values. The masses for HD 179949 b and τ Boo b were derived from $M_p \sin i$, stellar rotational periods, $v \sin i$, and orbital inclination assuming alignment with the stellar spin axis. The radii for HD 179949, τ Boo b, and υ And b were estimated using a probabilistic mass-radius relationship[56]. Significant differential rotation has been noted for τ Boo[53] and HD 179949[48]. Here we take the rotation period for the polar latitudes in both systems.

Object	mean($F_{\rm K}$) (10^4 erg cm^{-2} s^{-1})	max($F_{\rm K}$) (10^4 erg cm^{-2} s^{-1})	mean($P_{\rm K}$) (10^{20} W)	max($P_{\rm K}$) (10^{20} W)	$\phi_{\rm max}$
HD 179949	6.67 ± 1.18	$10.76^{+0.28}_{-0.28}$	1.53 ± 0.27	$2.46^{+0.13}_{-0.13}$	$0.65^{+0.01}_{-0.01}$
HD 189733	3.22 ± 0.77	$5.76^{+0.62}_{-0.63}$	0.28 ± 0.07	$0.49^{+0.09}_{-0.09}$	$0.92^{+0.02}_{-0.02}$
τ Boo	1.25 ± 0.35	$2.43^{+0.12}_{-0.12}$	0.41 ± 0.11	$0.79^{+0.08}_{-0.08}$	$0.77^{+0.02}_{-0.02}$
υ And	2.64 ± 0.44	$4.25^{+0.10}_{-0.10}$	1.14 ± 0.19	$1.84^{+0.11}_{-0.11}$	$0.46^{+0.01}_{-0.01}$

Table 2: **Ca II K absolute fluxes (F_K) and powers (P_K).** The uncertainties on the mean flux and mean power are the standard deviation of the mean for each phased SPI signal. The uncertainty for the maximum flux is the 1-σ error for the individual value. Uncertainties on the maximum power and peak phase are derived from the MCMC sinusoid fitting (see Methods). The sub-planetary point is taken to be where $\phi = 0$.

$\epsilon = E_{\rm CaIIK}/E_{\rm tot}$	HD 189733 b	HD 179949 b	τ Boo b	υ And b
100%	0.4 ± 0.1	1.9 ± 0.7	2.7 ± 0.9	1.9 ± 1.8
0.12%	27 ± 8	111 ± 38	163 ± 52	118 ± 109
0.20%	20 ± 7	86 ± 29	117 ± 38	83 ± 77
0.28%	17 ± 5	68 ± 23	95 ± 30	68 ± 63
Yadav & Thorngren (2017)	53 ± 17	89 ± 31	213 ± 52	62 ± 30

Table 3: **Surface polar planetary magnetic field ($B_{\rm p0}$) strengths.** Magnetic fields are calculated using the flux tube model from equation (2) and the extra heat deposition theory[38]. Field strengths are given in units of Gauss. All uncertainties are 1-σ values and are derived by combining the various parameter uncertainties from equation (2) in quadrature.

Supplementary tables and figures. Supplementary information including a log of the observations (Supplementary Table 1) and graphics showing the flux calibration method (Supplementary Figures 1 - 3).

Object	Observation Date	Instrument	Telescope	$\lambda/\Delta\lambda$	Reference
HD 179949	2001 Aug 25	Gecko	CFHT	110,000	12
	2001 Aug 26	Gecko	CFHT	110,000	
	2001 Aug 28	Gecko	CFHT	110,000	
	2002 Jul 25	Gecko	CFHT	110,000	
	2002 Jul 28	Gecko	CFHT	110,000	
	2002 Jul 29	Gecko	CFHT	110,000	
	2002 Aug 20	Gecko	CFHT	110,000	
	2002 Aug 22	Gecko	CFHT	110,000	
	2005 Sep 16	ESPaDOnS	CFHT	80,000	15
	2005 Sep 20	ESPaDOnS	CFHT	80,000	
	2005 Sep 21	ESPaDOnS	CFHT	80,000	
HD 189733	2013 Aug 4	NARVAL	TBL	65,000	16,48
	2013 Aug 5	NARVAL	TBL	65,000	
	2013 Aug 8	NARVAL	TBL	65,000	
	2013 Aug 10	NARVAL	TBL	65,000	
	2013 Aug 11	NARVAL	TBL	65,000	
	2013 Aug 13	NARVAL	TBL	65,000	
	2013 Aug 15	NARVAL	TBL	65,000	
	2013 Aug 18	NARVAL	TBL	65,000	
	2013 Aug 19	NARVAL	TBL	65,000	
	2013 Aug 21	NARVAL	TBL	65,000	
	2013 Aug 22	NARVAL	TBL	65,000	
τ Boo	2006 Jun 9	ESPaDOnS	CFHT	80,000	15
	2006 Jun 10	ESPaDOnS	CFHT	80,000	
	2006 Jun 12	ESPaDOnS	CFHT	80,000	
	2006 Jun 13	ESPaDOnS	CFHT	80,000	
	2006 Jun 14	ESPaDOnS	CFHT	80,000	
	2006 Jun 15	ESPaDOnS	CFHT	80,000	
	2006 Jun 16	ESPaDOnS	CFHT	80,000	
	2006 Jun 17	ESPaDOnS	CFHT	80,000	
	2006 Jun 18	ESPaDOnS	CFHT	80,000	
υ And	2002 Jul 27	Gecko	CFHT	110,000	13
	2002 Jul 28	Gecko	CFHT	110,000	
	2002 Jul 29	Gecko	CFHT	110,000	
	2002 Jul 30	Gecko	CFHT	110,000	
	2002 Aug 21	Gecko	CFHT	110,000	
	2002 Aug 23	Gecko	CFHT	110,000	
	2003 Sep 9	Gecko	CFHT	110,000	
	2003 Sep 10	Gecko	CFHT	110,000	
	2003 Sep 11	Gecko	CFHT	110,000	
	2003 Sep 12	Gecko	CFHT	110,000	
	2003 Sep 13	Gecko	CFHT	110,000	

Supplementary Table 1: Log of observations. Note that all raw and calibrated data are available from the CFHT (https://www.cadc-ccda.hia-iha.nrc-cnrc.gc.ca/en/cfht/) and PolarBase (http://polarbase.irap.omp.eu/) archives.

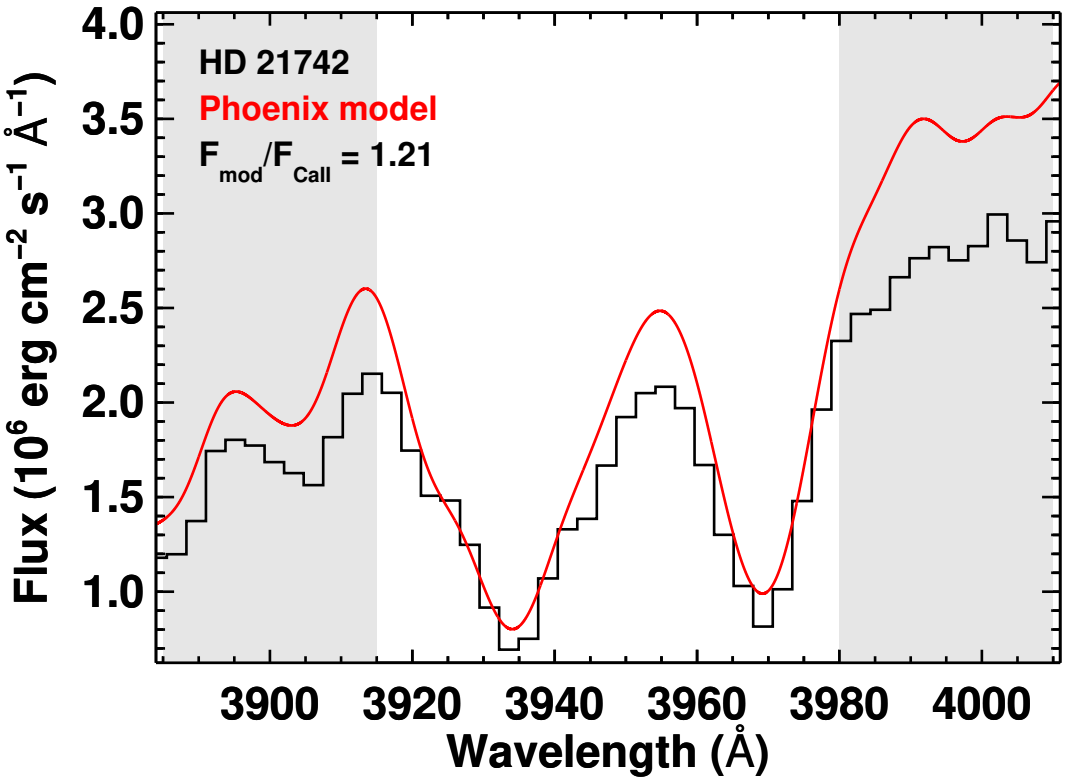

Supplementary Figure 1: Example of the NGSL star HD 21742 and the PHOENIX model spectrum of the same $T_{\rm eff}$. The value of the ratio plotted in the bottom panel of Supplementary Figure 2 is given in the upper-left. The continuum bands used for the mean flux comparison are shown with the shaded gray areas.

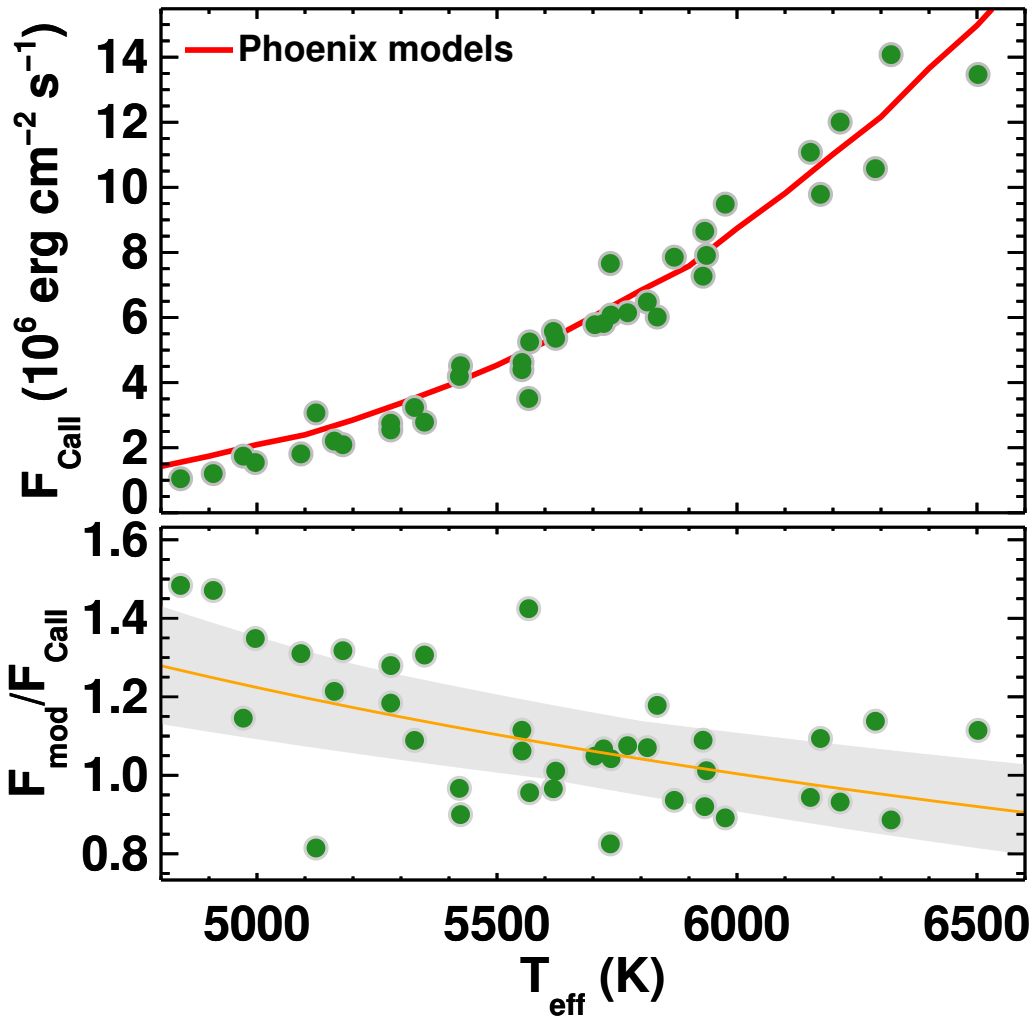

Supplementary Figure 2: Top panel: surface fluxes for the selected NGSL sample (green circles) and the flux values from the PHOENIX model spectra (solid red line). Bottom panel: the ratio of the model fluxes to the measured fluxes. The PHOENIX models tend to over-predict the surface fluxes for $T_{\rm eff} \lesssim 5500$ K. A power-law fit to this trend is shown with the orange line, as well as the 68% confidence intervals in the banded gray region. The power law fit is used as a corrective factor when applying the PHOENIX models to our SPI targets.

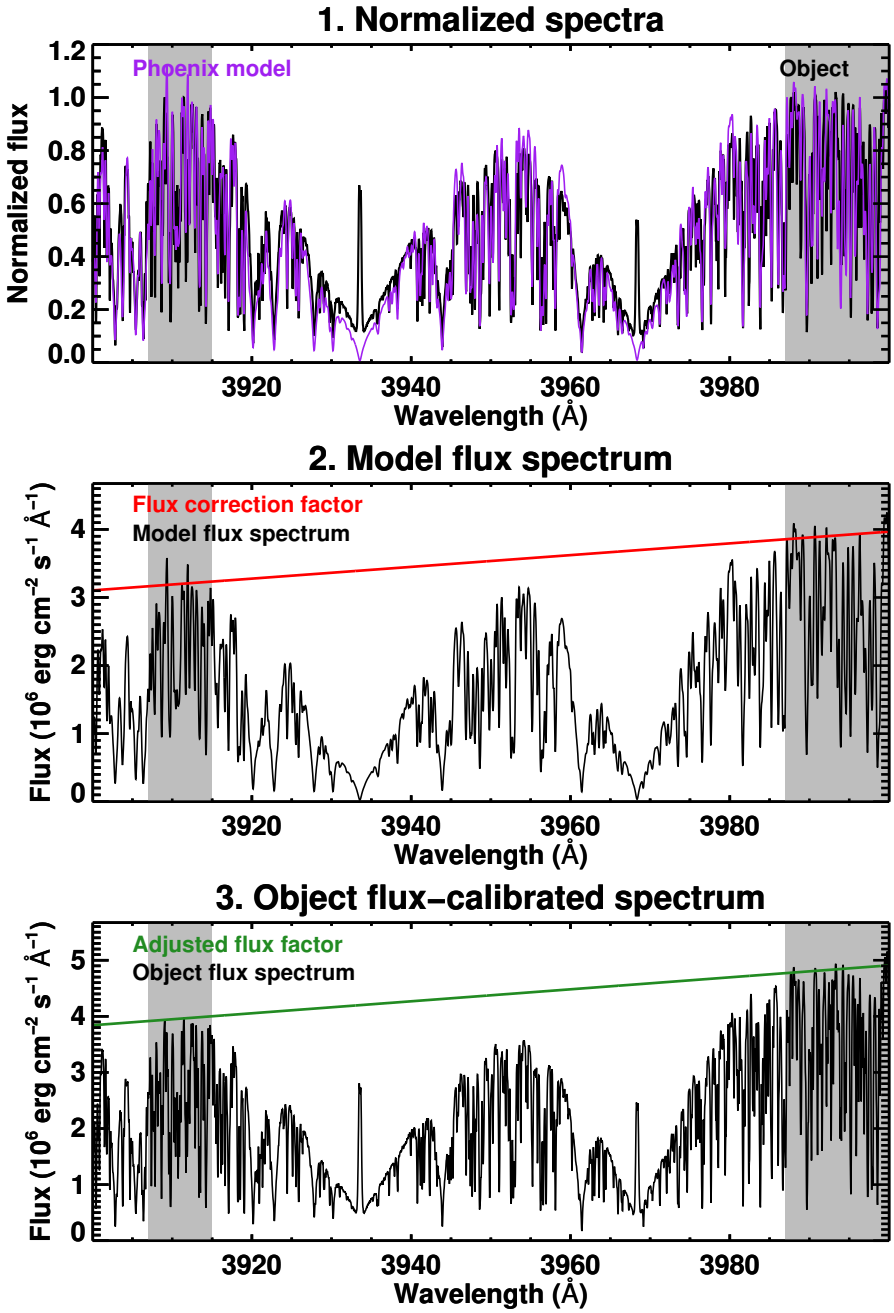

Supplementary Figure 3: Step-by-step visualization of the flux calibration process. The gray bands in all panels show the range of wavelengths used to normalize the spectra or fit the continuum flux. The left panel shows the normalized spectrum comparison between the object and the rotationally broadened PHOENIX model of the same $T_{\rm eff}$. The middle panel shows the linear flux continuum fit (red line) to the PHOENIX model flux spectrum. The third panel shows the flux continuum fit (green line) to the model spectrum, adjusted for the power law correction shown in Supplementary Figure 2, and the flux calibrated object spectrum.